COMMUNICATIONS PHYSICS

ARTICLE

https://doi.org/10.1038/s42005-019-0208-7 OPEN

High-accuracy bulk electronic bandmapping with eliminated diffraction effects using hard X-ray photoelectron momentum microscopy

S. Babenkov [1], K. Medjanik[1], D. Vasilyev[1], S. Chernov[1], C. Schlueter[2], A. Gloskovskii[2], Yu. Matveyev[2], W. Drube[2], B. Schönhense[3], K. Rossnagel[2,4], H.-J. Elmers[1] & G. Schönhense [1]

A key benefit of angle-resolved photoelectron spectroscopy (ARPES) in the X-ray range is the significant increase of the information depth, thanks to the large inelastic mean-free-path of the escaping photoelectrons. In practice hard X-ray ARPES (HARPES) faces severe challenges by low cross sections, large photon momentum transfer, and in particular strong phonon scattering and photoelectron diffraction effects. Here, we show that these challenges can be overcome by extending ultra-efficient time-of-flight momentum microscopy into the hard X-ray regime. Phonon scattering destroys the initial momentum distribution but subsequent diffraction at the lattice imprints a pronounced Kikuchi-type pattern on the background signal. Moreover, the pattern of the valence electrons is modulated by diffraction as well. For the examples of the medium-weight element materials Mo and layered $TiTe_2$, we demonstrate how comprehensive valence-band and core-level photoemission data taken under identical conditions can be used to effectively remove photoelectron diffraction effects in HARPES band maps.

[1] Johannes Gutenberg-Universität, Institut für Physik, 55099 Mainz, Germany. [2] Deutsches Elektronen-Synchrotron DESY, 22607 Hamburg, Germany. [3] Imperial College, Department of Bioengineering, London SW7 2AZ, UK. [4] Christian-Albrechts-Universität zu Kiel, Institut für Experimentelle und Angewandte Physik, 24098 Kiel, Germany. Correspondence and requests for materials should be addressed to G.S. (email: schoenhe@uni-mainz.de)

The increasing availability of high-brilliance soft and hard X-ray beams at synchrotron sources has launched angle-resolved photoelectron spectroscopy (ARPES) of a new generation[1–6]. Genuine bulk electronic structure information can be gained, solving the surface sensitivity problem of low-energy ARPES. Soft X-ray ARPES at photon energies of typically less than 1000 eV, corresponding to information depths up to 5 nm[7], is now a standard method at modern synchrotron radiation sources that has recently been stretched to in-depth studies of novel topological materials[8–10], bulk impurities[11], buried interfaces[12], and device-like heterostructures[13]. The information depth is further increased in the hard X-ray range, reaching ~20 nm at $h\nu = 6$ keV (ref. [7]). In this truly bulk-sensitive regime, only a few ARPES experiments have been performed up to now[4,5,14,15].

This rareness of such experiments is because the desired increase of the inelastic mean-free-path λ_{IMFP} in hard X-ray ARPES (HARPES) comes along with several effects that hamper photoemission at high energies. The approximated wavelength of the final-state wavefunction $\lambda_e = 2\pi/k_f$ varies from 61 to 15.8 pm in the region between 400 eV and 6 keV. This has two important consequences. First, the photoionization cross- sections drop strongly since the shorter wavelength leads to cancellations in the overlap integral of the transition matrix elements. Between 400 eV and 6 keV most subshell cross- sections go down by several orders of magnitude[16]. Second, λ_e shorter than interatomic distances gives rise to core-like X-ray photoelectron diffraction (XPD), leading to pronounced intensity modulations in angle or momentum.

Another serious effect, which can smear out all band-structure information, is electron-phonon scattering. Due to the increasing mean-free- path, the cross-section of this process increases with kinetic energy, and it becomes the dominant loss channel in high-energy photoemission. Phonon scattering can transfer large momenta, while energy transfer is typically limited to <100 meV. Hence, the photoelectron momentum distribution becomes "randomized" resulting in a strong diffuse background. The characteristic spectral distribution of this background reflects the matrix-element-weighted density of states (MEWDOS), as observed and discussed in previous work[17–21]. Similar to diffraction experiments, the relative weight of the phonon-scattering channel essentially depends on a photoemission Debye–Waller factor. Debye–Waller criteria in fact appear to rule out most materials for HARPES[22,23]. In reasonable agreement with theory[24], however, well-resolved band-structure features have been measured up to 6 keV for tungsten[4], which represents a special case because it is heavy ($Z = 74$) and has a high Debye temperature (377 K). Due to its high Debye–Waller factor at cryogenic temperatures, tungsten is less prone to phonon smearing effects in HARPES than most other materials.

Overall, low cross-sections, pronounced photoelectron diffraction, strong phonon scattering, and also large photon momentum transfer to the photoelectron render HARPES a challenging task. Here, we present an approach that eliminates the strong inherent distortions in the measured HARPES band maps originating from these effects. The medium-Z metal Mo ($Z = 42$) and the reference transition-metal dichalcogenide $TiTe_2$ serve as examples from a comprehensive series of measurements on various materials with photon energies up to 6 keV. The experiments are carried out with a time-of-flight momentum (k) microscope[6] at beamline P22 of the storage ring PETRA III at DESY in Hamburg (Germany), providing hard X-rays with one of the highest brilliances worldwide in an energy range from 2.4 to 15 keV[25]. For comparison, data taken in the soft X-ray range are included (for details on beamlines and microscope, see Methods section). The simultaneous measurement of valence-band momentum maps and core-level photoelectron diffraction patterns, taken at identical settings of the microscope (kinetic energy, k-field of view), allow the quantitative correction of the diffraction modulation in the as-measured valence- band patterns.

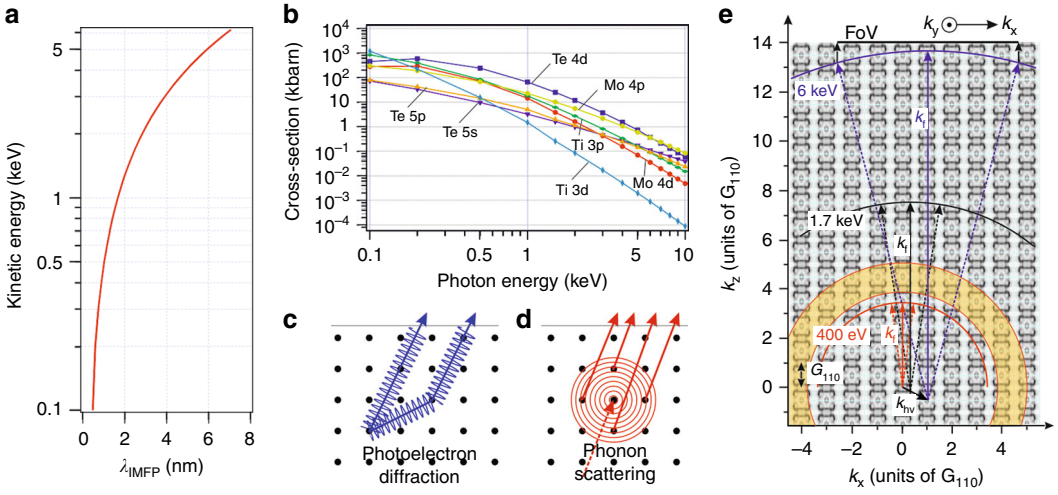

Fig. 1 Advantage and challenges of hard X-ray photoemission for the examples of Mo and $TiTe_2$. **a** The advantage of high kinetic energies in terms of increased information depth, quantified by the inelastic mean-free-path λ_{IMFP}. Since 90% of the signal originate from ~$3\lambda_{\mathrm{IMFP}}$, the information depth reaches 20 nm at 6 keV[7]. **b**–**d** Three challenges of hard X-ray photoemission: dropping photoionization cross-section[16] (**b**), photoelectron diffraction (**c**), and phonon scattering (**d**); wavelength to scale for 3 keV electrons in an Mo lattice. **e** Quantitative scheme of valence-band photoemission from Mo(110) into free-electron-like final states between $h\nu = 400$ eV and 6 keV. Momentum components k_x and k_z are quantized in multiples of the reciprocal lattice vector $G_{110} = 2.824$ Å^{-1}. The final-state sphere of radius k_f (here plotted for emission from the Fermi level (E_F)) runs through a large k-range between the third and 14th repeated Brillouin zone. Its center is displaced from the origin $\boldsymbol{k} = (0,0,0)$ by the photon momentum $\boldsymbol{k}_{h\nu}$. Dashed vectors indicate the range observed by the k-microscope (field of view (FoV) indicated on top); the vector $\boldsymbol{k}_f$ denotes emission normal to the surface. The background pattern shows a $k_y = 0$ cut (at E_F) of the periodically repeated measured spectral density; dark denotes high spectral density. The spectral function was mapped in the yellow area with small steps of 0.1 Å^{-1} along k_z via appropriate setting of many photon energies

Results

Molybdenum (110). Figure 1a, b shows the inelastic mean-free-path and the partial cross-sections of Mo 4*d* and 4*p*, respectively, revealing the enhancement of the information depth ($\sim 3\lambda_{\mathrm{IMFP}}$) and the strong drop in subshell cross-sections with increasing energy. Figure 1c, d illustrates the effects of photoelectron diffraction and phonon scattering, respectively, with the wavelength to scale for 3 keV electrons in Mo.

Figure 1e shows a quantitative transition scheme for Mo, assuming direct transitions into free-electron-like final states. In the extended zone scheme, these are located on a sphere with radius

$$k_{\mathrm{f}}\,(\mathrm{\AA}^{-1}) \sim 0.512\sqrt{(E_{\mathrm{final}}\,(\mathrm{eV}))(m_{\mathrm{eff}}\,(\mathrm{m}))} \quad \text{with} \quad E_{\mathrm{final}} = h\nu - E_{\mathrm{B}} + V_{\mathrm{o}}^{*}, \tag{1}$$

where m_{eff} and m are the effective mass and free-electron mass, E_{B} and $V_0{}^*$ the binding energy and inner potential, both referenced to the Fermi level (E_{F}).

Photons with energies between 400 eV and 6 keV induce transitions into the third to 14th repeated Brillouin zone (BZ). The photon wave vector $\boldsymbol{k}_{h\nu}$ is transferred to the photoelectron, causing a displacement of the center of the sphere. For 6 keV, this shift ($k_{h\nu} = 2\pi\nu/c = 3.178\ \mathrm{\AA}^{-1}$) is larger than the diameter of a full BZ. The periodic background pattern in Fig. 1e is a cut of the measured 3D spectral density function at E_{F} in the plane of photon incidence (k_z–k_x). The intersection of the final-state sphere with the spectral function reveals where band features appear under arbitrary emission directions. Note that the *k*-scale of Fig. 1e is aligned with the energy scale of Fig. 1a, showing the inelastic mean-free- path λ_{IMFP} for Mo which increases from 0.5 to 6.8 nm in this range.

The top row of Fig. 2a–d shows the as-measured *k*-distributions (sections at E_{F}) from an Mo(110) crystal at four selected final-state energies between 3110 and 6010 eV. Up to the maximum photon energy, sharp band features are visible in the imaged *k*-region of $\sim 12\ \mathrm{\AA}^{-1}$ diameter. In particular, we recognize the diamond-shaped electron pockets at the Γ-points (labeled A), the spherical electron pockets (B) at the corners of diamond A, the elliptical contour of the hole pockets centered at the N-points (C) and the octahedron-shaped electron pocket centered at the H-points (D) as denoted in the calculated and measured Fermi surface. However, intense background patterns with characteristic shapes are superimposed on the *k*-distributions in the top row.

Assuming that the structured background patterns in Fig. 2a–d are the fingerprint of XPD, we took high-resolution diffraction patterns of the shallow Mo 4*p* core level at the same kinetic energies by varying slightly the photon energy, and using identical settings of the microscope, assuring the same *k*-field of view. The results are shown in Fig. 2e–h. The small-angle diffractograms exhibit rich structure with the finest features corresponding to an angular width of <0.1° only. The diffraction features show a strong variation with photon energy and get more detailed with increasing energy (see sequence of Fig. 2e–h).

Although it comprises a number of BZs as marked in Fig. 2b, the *k*-field of view (see scale bars) corresponds to a rather small polar angular range of ~10°. This is the reason why the characteristic strong XPD signals from forward-scattering along atom rows[26,27] are missing. Nevertheless, we identify the fingerprint of the crossing region of the central Kikuchi bands[28]. The dominant orthogonal Kikuchi bands are indicated by dashed lines in Fig. 2h. The horizontal band is marked by arrows and the center of the XPD pattern by a plus sign in Fig. 2e–h. The center is the crossing region of two orthogonal Kikuchi bands. The expected two-fold symmetry of the (110)-surface is broken by the incoming *p*-polarized photon beam. The photon momentum is denoted by the arrow in Fig. 2d; the electric-field vector is oriented 22° off-normal. These Kikuchi bands arise from Bragg scattering on lattice planes perpendicular to the surface. Owing to the relatively large scattering factor of Mo, the Kikuchi band is not as sharp as for light elements, but sufficiently clear for an identification of the relevant reciprocal lattice vector $\mathbf{G}_{001}$. The width of the band is approximately $2G_{001}$. In addition, we recognize dark excess lines and edges of Kikuchi bands with their characteristic sharp intensity jump (Fig. 2h, bottom left). Indeed both the dark line and the edges are visible in the as-measured valence-band distribution as well (Fig. 2d, bottom left).

The shifts of the field of view result from small movements of the photon footprint on the sample when changing the photon energy. In order to retain identical settings, these shifts were not corrected by electron beam deflection. Remarkably, the prominent features in the Mo 4*p* core-level diffractograms (Fig. 2e–h) appear to be identical to the background features in the valence-band patterns (Fig. 2a–d). In particular, the crossing Kikuchi bands indicated by the dashed lines in Fig. 2h appear also in Fig. 2d. Assuming that the background intensity carries the XPD signature, we subtract the diffractograms of Fig. 2e–h from the valence-band patterns in Fig. 2a–d, introducing an empirical weighting factor. The (pixel-by-pixel) difference images of the valence-band patterns and the weighted Mo 4*d* XPD patterns measured at identical kinetic energies are shown in Fig. 2i–l. The background features are largely removed, leaving a residual background with much less intensity (the image contrast in Fig. 2i–l is enhanced for sake of visibility of faint structures).

Surprisingly, the difference images in Fig. 2i–l still show intensity enhancements due to XPD in the valence-band patterns themselves. For example, the intense feature marked by arrows in Fig. 2j obviously falls on a high-intensity region in the corresponding diffractogram of Fig. 2f. Apparently, the valence-band electrons originating from *k*-conserving direct transitions into free-electron- like bands carry a diffraction signature resembling the core-level XPD patterns. Assuming that the intensity modulation is correlated with the one seen in the XPD patterns measured for the core level, we try a multiplicative correction in terms of a pixel-by-pixel division of the raw data in Fig. 2a–d by the XPD patterns in Fig. 2e–h. The result is shown in the fourth row (Fig. 2m–p). Clearly, the XPD signature of the background is better removed in Fig. 2m–p suggesting that the background intensity has been divided by itself yielding just a constant intensity offset. In addition, the valence-band map is further homogenized in comparison with the purely subtractive correction (Fig. 2i–l), because the multiplicative correction also eliminates detector artefacts.

Figure 2q–t shows E_{B}-vs-*k* sections through the corrected arrays of Fig. 2m–p, cut along the dashed lines. These cuts clearly reveal the band dispersions which in the uncorrected arrays would be partly masked by the imprinted XPD modulation. Note that the spectral distribution of the background following the MEWDOS[17–21] is largely eliminated at the lower energies (Fig. 2q, r). However, residues of horizontal stripes, characteristic for the MEWDOS background, are still visible at 5410 eV (Fig. 2s). The inhomogeneity in these residual stripes point on a (small) *k*-dependence of the MEWDOS background. At 6010 eV a diffuse background is underlying the band pattern on the right-hand side, reflecting the dramatic drop in the fraction of non-scattered photoelectrons (see below) and an increase of inelastic scattering at such high energies as we will discuss below.

Figure 2u, v shows the intensity spectra integrated over the field of view for the valence band and the Mo 4*p* signal, respectively. Figure 2w, y displays the calculated and measured Fermi surface of Mo, respectively.

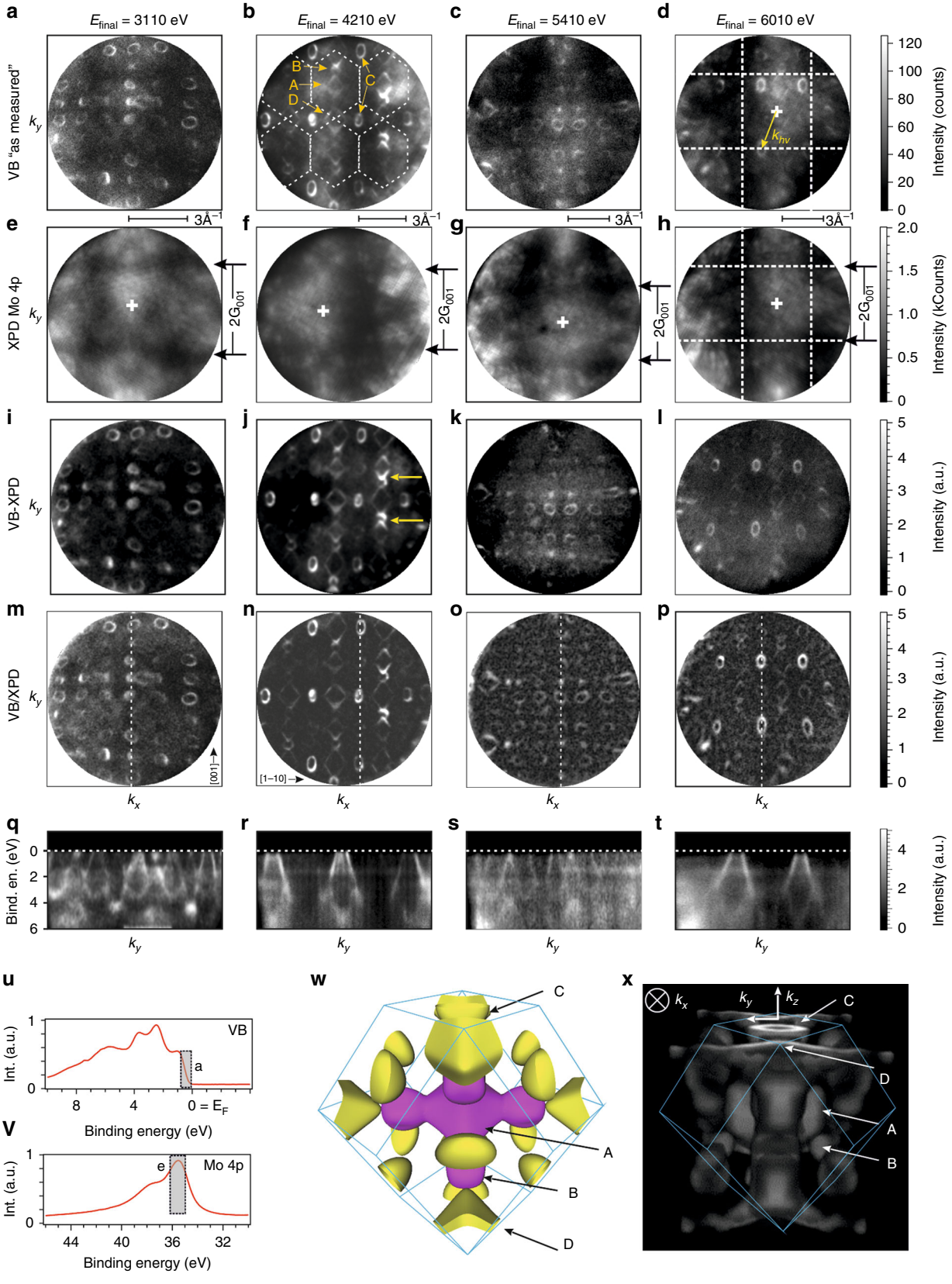

Close inspection of Fig. 2m–p reveals that there are still various regions of significant local intensity enhancement. This resembles our earlier result found in the soft X-ray range[29]. We will come back to this point in the Discussion section.

Bandmapping of $TiTe_2$. Figure 3 presents HARPES data for $TiTe_2$, a layered Fermi-liquid reference compound[30] of the family of transition-metal dichalcogenides. In the as-measured valence-band map (Fig. 3a) band features are hardly discernible as the pattern is dominated by the pronounced sixfold star-like shape

Fig. 2 Results for Mo(110) at photon energies between 3.1 and 6 keV, corresponding to the final-state energies given on top. **a**–**d** As-measured large-area momentum maps of valence bands (VB) (sections at the Fermi level). Dashed lines in **b** denote the Brillouin zones (approximately because of the curved final-state sphere). A denotes the diamond-shaped electron pocket at the Γ-point, B the electron balls at the corners of the diamond, C the ellipsoidal hole pockets at the N-points, and D the octahedron-shaped electron pockets at the H-points, altogether making up the Fermi surface. **e**–**h** High-resolution 4*p* core-level diffraction patterns taken at identical final-state energies as **a**–**d**; arrows mark the central Kikuchi band[28]. The scales of the *k*-fields are identical in rows one and two, but vary slightly with energy as denoted by the scale bars; intensity in counts per pixel. **i**–**l** Same distributions as top row after subtraction of the core-level patterns from the second row, weighted by an empirical intensity factor. **m**–**p** Same distributions as top row after pixel-by-pixel division by the core-level patterns from the second row. **q**–**t** E_B-vs-*k* sections through the arrays of the fourth row along the dashed lines. **u**, **v** Momentum-integrated spectra corresponding to **a, e**, respectively. **w** Brillouin zone with calculated Fermi surface (from ref. [41]). **x** Fermi surface of Mo measured in a photon-energy interval between 400 and 900 eV using the method described in ref. [6]

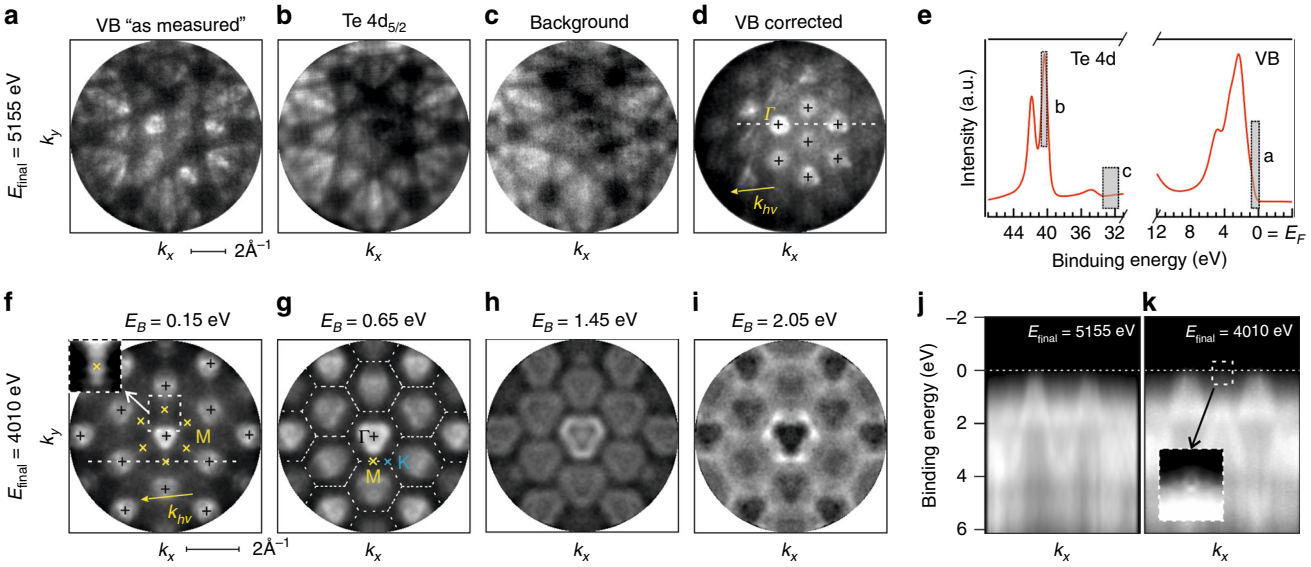

Fig. 3 Momentum-resolved hard X-ray photoemission from $TiTe_2$. Results for final-state energies of 5155 eV (**a**–**d**) and corresponding intensity spectrum (**e**). Binding energy sequence for final-state energy of 4010 eV (**f**–**i**). The as-measured valence-band (VB) pattern at the Fermi level (**a**) looks similar to the diffractograms of Te 4*d* (**b**) and the flat background away from the core-level signals (**c**). After correction, the strong diffraction modulation has disappeared (**d**). **e** Corresponding momentum-integrated spectra, the energy regions, over which the *k*-maps **a**–**d** were integrated, are marked by bars. **f**–**i** Constant-energy maps at different binding energies E_B (integrated over intervals of ±0.15 eV corresponding to the photon bandwidth). The Brillouin zones and high-symmetry points are denoted in **g**; $\boldsymbol{k}_{h\nu}$ indicates the photon-momentum vector. **j**, **k** E_B-vs-*k* sections along the Γ-M-Γ direction; the electron pocket at the M-point is shown in the inset with increased contrast (dashed rectangle). All momentum scales in **a**–**d**, **f**–**k** have identical sizes as defined by the scale bars in **a, f**

found in the XPD patterns at this energy. Figure 3b, c shows the XPD patterns of the Te 4*p* core level and the background at the high-energy end of the spectrum. This background can be viewed as the weighted average of diffraction from the Te and Ti sublattices. Since Te is much heavier ($Z = 52$ vs $Z = 22$ for Ti), the dominant contribution is given by diffraction from the Te sublattice. The corrected pattern shown in Fig. 3d has been obtained by pixel-by-pixel division of the raw data (Fig. 3a) by the Te $4d_{5/2}$ XPD pattern (Fig. 3b). It reveals a clear valence-band map at E_F; the strong diffraction artefacts have completely disappeared. The spectral regions over which the maps in Fig. 3a–c have been integrated are marked in the spectra displayed in Fig. 3e.

The bottom row (Fig. 3f–i) shows energy isosurfaces for different binding energies E_B as given in the panels. The same data processing as for Fig. 3d (division by the Te $4d_{5/2}$ XPD pattern) has been applied to the energy cuts shown in Fig. 3f–i. The band features are pronounced, distortion-free, and exhibit the threefold symmetry of the 1*T* structure. The band dispersion is displayed in the E_B-vs-*k* sections shown in Fig. 3j, k. These panels show cuts through the corrected data arrays for $E_{final} =$ 5155 eV (along the dashed line in Fig. 3d) and 4010 eV (along the dashed line in Fig. 3f). Similarly to the high-energy results (Fig. 2s, t), we recognize residues of MEWDOS stripes and a rather large diffuse background in the E_B-vs-*k* sections. The onset of this diffuse background at $E_B > 0.5$ eV originates from energy-loss processes like electron–hole excitations in the valence band. The region in close vicinity of the Fermi level is free of this inelastic background contribution.

Besides the intense circular Te 5*p*-derived features at the Γ-points, the Fermi surface map should contain Ti 3*d*-derived elliptical electron pockets at the M-points, midway between two adjacent Γ-pockets. However, the Ti 3*d* ellipses cannot be identified in the $E_{final} = 5155$ eV patterns (Fig. 3d, j) illustrating the larger relative cross- section for initial states of *s*- and *p*-character over states with *d*- and *f*-character in HARPES[16]. In addition to the low Ti 3*d* cross-section (Fig. 1b), these pockets are only about 200 meV deep[31], smaller than the photon bandwidth. Overall, the low cross-section (two orders of magnitude lower than all others in Fig. 1b), the low Z ($Z = 22$) and the small spectral range (200 meV) of the Ti 3d-derived pockets pose a high challenge on the detection of this feature in HARPES. We find the onset of visibility at $h\nu = 4000$ eV, as shown in Fig. 3f, k, where the regions around the pocket are displayed with increased contrast. The pockets exhibit the characteristic elongated shape (Fig. 3f) and appear stretched in energy due to the photon bandwidth (Fig. 3k).

Discussion

The structured background patterns in Figs. 2a–d and 3a originate from a combined action of phonon scattering and diffraction. Phonon scattering is a stochastic process, which destroys the initial k-distribution of the electrons, leading to a (statistical) randomization of the k-vector. The change in energy (<100 meV) is smaller than the photon bandwidth, hence the scattered electrons cannot be separated energetically from the true signal. These electrons have lost their memory on the initial k-distribution. However, they are diffracted at the lattice, analogously to the well-known Kikuchi-type diffraction in scanning electron microscopy (SEM). The Kikuchi bands observed in backscattering in SEM[28] also appear due to initial scattering events at phonons and diffraction of these background electrons at the lattice. In the wave picture, the scattered electrons are described as spherical waves centered at the location of the stochastic event. An important result of the present paper is that the strong background signal in high-energy photoemission, originating from phonon scattering, also carries this Kikuchi-type diffraction signature.

Kikuchi patterns are characteristic for the diffraction of a spherical wave generated inside of the material by a scattering event. The diffraction pattern depends on the photoelectron wavelength, i.e., on E_{final}, which can be considered as the photoelectron kinetic energy inside of the material. The primary signal can be a high-energy electron beam in an electron microscope or an electron in a high-energy Bloch wave generated by a direct transition from an itinerant band state. Even other inelastic processes in solids can generate spherical waves that undergo diffraction. This is in accordance with the fact that also the inelastic background on the high-energy side of the core-level signal displays an XPD pattern[32,33] (an example is shown in Fig. 3c). Photoemission from localized band states or core levels (point emitters) also leads to an outgoing spherical wave. Hence such photoelectrons can experience Kikuchi-type diffraction as well[26,27,34], even without phonon scattering processes being involved (although in practice these are always present at finite temperatures). At identical final-state energies the observed momentum patterns in all these cases look alike because the underlying process, a spherical wave being diffracted at the lattice, is the same.

The equivalence of the diffraction patterns imprinted on the quasi-elastic background in valence- band k-maps and the XPD patterns of electrons from core levels at the same final-state energy can be exploited for an effective elimination of the background. Either the core-level XPD pattern is subtracted from the as-measured valence pattern using an intensity factor as empirical parameter, or the valence pattern is divided by the XPD pattern leading to a homogeneous background that can easily be subtracted. Both procedures lead to similar results (compare Fig. 2i–l with Fig. 2m–p), the division effectively also removes detector artefacts.

The Debye–Waller formalism quantifies the fraction of photoemission intensity originating from direct transitions without phonon scattering. The Debye temperatures[35] of Mo and $TiTe_2$ are 423 and 217 K, respectively. Figure 4 depicts the fraction of k-conserved photoelectron intensity at $T = 30$ K of the Mo(110) and $TiTe_2$ valence bands that cross the Fermi level near the N point (for Mo) and Γ-point (for $TiTe_2$) as a function of E_{final} in a semi-logarithmic plot. The fraction of k-conserved valence- band intensity for each kinetic energy results from $I_{\mathrm{VB}} = (I_{\mathrm{max}} - I_{\mathrm{B}})/I_{\mathrm{max}}$, where I_{max} and I_{B} denote the measured intensity at the N- (Γ-) point maximum and the averaged background intensity in close vicinity to the corresponding N- and Γ-point, respectively. The division by I_{max} accounts for different accumulation times and X-ray intensity for the individual measurements. We have used processed data similar to the data shown in Fig. 2m–p in order to eliminate the diffraction contribution.

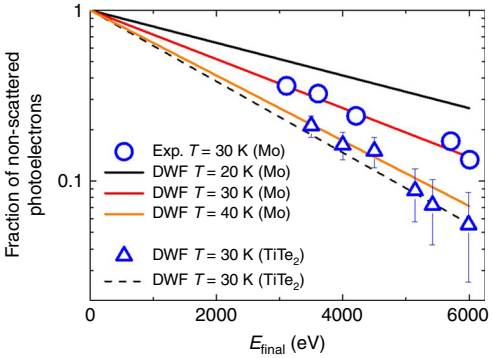

Fig. 4 Debye–Waller factor analysis. Semi-logarithmic plot of the photoemission intensity of the Mo (blue circles) and $TiTe_2$ (blue triangles) valence band close to the Fermi level versus final-state energy at 30 K. The data near the N point of Mo(110) has been normalized to the extrapolated value at $E_{\mathrm{final}} = 0$. The same normalization factor has been used for the case of $TiTe_2$. The low Z of Ti and lower Debye temperature of $TiTe_2$ leads to a dramatic drop of the fraction of k-conserved photoelectron intensity with increasing energy. Full lines, Debye–Waller factor for Mo as a function of final-state energy for indicated sample temperatures

One expects a decreasing intensity with increasing final-state energy as described by the Debye–Waller factor[34] $\mathrm{DWF} = \mathrm{e}^{-\alpha T E_{\mathrm{final}}}$. The fitted value $= (1.1 \pm 0.1) \times 10^{-5}\,\mathrm{K}^{-1}\,\mathrm{eV}^{-1}$ agrees with the predicted value $1.2 \times 10^{-5}\,\mathrm{K}^{-1}\,\mathrm{eV}^{-1}$ for Mo. Note that the prefactor α comprises an energy-independent factor averaged over all possible scattering paths[34]. The DWF represents within this model the probability p that one observes a direct transition without scattering event. Consequently, the probability of a scattering event with the loss of momentum information is $1 - p$. Since both observables originate from the same diffraction process, the procedure of division of the original data by the XPD pattern eliminates the modulation caused by diffraction both for the direct transition fraction and from the background intensity. Thus, one observes the valence band on a homogeneous background intensity, allowing for a quantitative evaluation of p. Our results confirm within error limits the predicted decrease with increasing photon energy of the valence- band intensity due to phonon scattering.

The temperature dependence becomes dramatic at high energies; at 6 keV the direct-transition signal drops by a factor of 4 upon a temperature increase from 20 to 40 K. For the case of $TiTe_2$ we determine the value $= (1.6 \pm 0.5) \times 10^{-5}\,\mathrm{K}^{-1}\,\mathrm{eV}^{-1}$. From the ratio of the Debye temperatures and atomic masses, one would expect a value of $= 2.2 \times 10^{-5}\,\mathrm{K}^{-1}\,\mathrm{eV}^{-1}$.

We assume that α is a constant, depending exclusively on the Debye temperature and the mass of the nuclei. In the rigorous formulation, the exponent of the DWF comprises the factors g^2 and u^2, where g is the relevant reciprocal lattice vector and u is the averaged amplitude of lattice vibrations. Note that the first factor is in fact not a constant for diffracted electrons, where one has to consider the reciprocal lattice vector involved in the diffraction. The averaging of the vibration amplitudes is not allowed in cases of strongly anisotropic phonon distributions. In future investigations, the time-of-flight momentum microscope will allow the observation of temperature- and momentum-dependent variations of the background intensity, which may result in additional physical insights into the phonon distribution and the electron–phonon interaction.

It is evident that our normalization procedure suppresses part of the intensity modulations originating from photoemission

matrix element and, e.g., dipole selection rules might be less visible. At first sight it is surprising that the momentum patterns at high energies do not show significant dichroism effects. With increasing photon energy, higher multipole contributions in the photon operator beyond the electric dipole approximation become significant. These mask the classical dipole selection rules and corresponding dichroism effects (circular and linear dichroism in the angular distribution CDAD, LDAD). These dichroism effects are substantial in the VUV range[36] and soft X-ray range[37] and in very good agreement with theory based on the dipole approximation. In addition to these multipole contributions, the partial cross-sections drop more rapidly for higher orbital quantum numbers, see Fig. 1b. This different weighting of partial-wave matrix elements influences the dichroism and also the spin polarization[38] in the hard X-ray range.

Remarkably, both procedures for eliminating the XPD intensity modulations (Fig. 2i–l and Fig. 2m–p) result in *k*-maps that still exhibit inhomogeneous local intensities. These are a fingerprint of a different diffraction mechanism acting on the valence-band photoelectrons. Kikuchi patterns in the background signal arise due to coherence-destroying scattering processes or from emission from fully localized core levels, both leading to outgoing spherical waves. The spherical waves experience Kikuchi-type diffraction at the lattice leading to highly symmetric patterns aligned with the crystal lattice. High-symmetry directions in the Kikuchi patterns coincide with the corresponding crystallographic directions. Unlike core electrons and scattered electrons, the electrons originating from direct transitions from itinerant band states are plane waves propagating into the direction $\boldsymbol{k}_{\mathrm{final}}$. Figure 1e makes clear that the full 4D valence-band emission pattern $I(E_B, \boldsymbol{k})$ (with E_B being a continuum) is fundamentally different from the 3D emission pattern of electrons from a core level (at a given E_B). The most important difference originates from the transfer of the photon momentum to the valence photoelectron, leading to a displacement of the final-state sphere in periodic *k*-space (Fig. 1e). This displacement breaks the symmetry and leads to non-symmetric diffraction features. Considering the continuum of E_B, this diffraction scheme is equivalent to Laue diffraction with a continuum of X-rays. It can be described in terms of Umklapp processes on the displaced final-state sphere involving reciprocal lattice vectors. We have discussed and quantified this effect in the soft X-ray range[29]. The intensity enhancement can reach a factor of 5. This momentum-transfer description can be visualized in terms of a geometric model resembling the Ewald construction, however, with the final-state sphere being displaced by the photon momentum $\boldsymbol{k}_{h\nu}$.

In conclusion, using two medium-weight element materials as examples, Mo and $TiTe_2$, we have presented a powerful method for high-accuracy bulk electronic structure mapping using momentum-resolved hard X-ray photoelectron spectroscopy. The key ingredients are high-resolution valence-band maps and core-level diffractograms taken at exactly the same kinetic energy and *k*-range. This allows for voxel-by-voxel processing of the 3D data arrays and disentangling of the different distortion effects due to quasi-elastic phonon scattering and photoelectron diffraction. A strongly structured background underlying the valence-band maps originates from phonon scattering and shows the same XPD pattern as core-level photoelectrons of the same final-state energy. Scattered valence electrons and core electrons show Kikuchi-type XPD patterns because both are described by a point emitter inside of the crystal.

The equivalence of the background in the valence maps and the core level Kikuchi patterns offer two ways for elimination of the background signal. We have shown that the background can be removed either by subtraction of the corresponding core-level diffractogram, introducing an intensity factor as empirical parameter. Alternatively the structured background can be removed via division by the core-level diffractogram, leading to a constant intensity offset. A residual XPD modulation of the band patterns originates from Laue diffraction of the propagating planes waves. This type of valence-band photoelectron diffraction can be considered as a matrix-element effect and fingerprint of the inverse LEED state[39,40], which up to now was hardly accessible experimentally. The proposed correction scheme eliminates the scattering and XPD contribution effectively. The results were obtained with a highly efficient momentum microscope, but the principles and procedures are independent of the photoelectron detection scheme.

Methods

Sample preparation. The Mo(110) crystal was cleaned by repeated cycles of heating in oxygen at 1500 K followed by desorption of the surface oxide at 2000 K; the base pressure during experiment was 4×10^{-10} mbar. Prior to the soft X-ray measurements the surface quality was verified by LEED, and at HAXPES energies the bulk electronic bands have even been observed without initial preparation. The $TiTe_2$ sample was cleaved in UHV prior to transfer to the microscope chamber. The samples are inserted into an He-cooled (~20 K) sample stage on a high precision 6-axis hexapod manipulator. Besides lens voltages and data acquisition system all mechanical adjustment parameters (hexapod, frame position, apertures of the microscope) are fully remote controlled since the HAXPES setup is located in a closed hutch.

Beamlines. The experiments were carried out at beamlines P22 and P04 of the storage ring PETRA III at DESY in Hamburg (Germany). Owing to the high energy (6.0 GeV) and large size (2.3 km circumference) of PETRA III, P22 provides hard X-rays with the highest brilliance worldwide in an energy range from 2.4 to 15 keV. Present conditions (in the commissioning phase) were 2×10^{13} photons/s at 4–6 keV in a spot of about $10 \times 10\ \mu m^2$ using a Si(111) double-crystal monochromator[25]. The bandwidth varies from 350 meV in the 3 keV range to 500 meV at >6 keV for the Si(111) crystal, the Si(311) crystal yields a five times less bandwidth. At 5.3 keV we measured 450 and 155 meV experimental resolution for the two crystals, respectively. Beamline P04 provides circularly-polarized photons in the range from $h\nu = 260$ eV to ~2 keV with a resolution limit up to 4×10^4 (<30 meV at $h\nu = 1000$ eV) in a spot of <25 µm diameter. In the soft X-ray experiments we used bandwidths around 50 meV.

Instrument. Data were taken using the momentum-microscope technique recording data arrays at many photon energies at both beamlines, as described elsewhere[6]. For the measurements in the HAXPES range at P22 we used the same combination of full-field *k*-imaging with ToF detection as in previous experiments but with a new optics, optimized for high initial kinetic energies and large *k*-field of view. A novel type of objective lens can image large solid-angle intervals comprising many Brillouin zones in parallel. Two groups of zoom lenses shape and decelerate this large phase-space volume (high energy and large solid angle) and focus the *k*-image onto the detector, in this case a delay-line detector (DLD) with 80 mm active area. The ToF microscope with delay-line detector has an energy resolution of <20 meV, so the total resolution is essentially given by the photon bandwidth at both beamlines.

Data recording. 3D data arrays $I(E_B, k_x, k_y)$ in the valence range are recorded with acquisition times of typically 20 min, and the acquisition of core-level XPD patterns is faster. The two momentum coordinates (k_x, k_y) are observed by full-field *k*-imaging (via magnification of the reciprocal image in the backfocal plane of the objective lens). By recording the time coordinate (referenced to the photon pulse) of each individual counting event in the DLD, many binding energies E_B are taken simultaneously in a single exposure. Typically, energy intervals with typical widths of ~6 eV are acquired (without any scanning). For larger intervals the *k*-resolution is diminished due to the chromatic aberration of the lens system.

The 40-bunch filling pattern of the storage ring corresponds to a pulse period of 192 ns, which perfectly matches the 5 MHz count-rate capability of the DLD. Photon pulse widths are about 50 ps rms. The high parallelization of data acquisition and the high brilliance of the beamlines compensate for the dramatic decrease of photoemission cross-section with increasing photon energy. Count-rates exceeding 10^6 counts per second in an interval of ~15 eV have been obtained in the valence range at all photon energies used. For core-level recording attenuation of the X-ray beam was necessary.

Data availability

The data that support the findings of this study are available from the corresponding author upon reasonable request.

Received: 14 March 2019 Accepted: 1 August 2019
Published online: 10 September 2019

References

1. Claesson, T. et al. Angle resolved photoemission from $Nd_{1.85}Ce_{0.15}CuO_4$ using high energy photons: a Fermi surface investigation. *Phys. Rev. Lett.* **93**, 136402 (2004).
2. Kamakura, N. et al. Layer-dependent band dispersion and correlations using tunable soft X-ray ARPES. *Europhys. Lett.* **67**, 240–246 (2004).
3. Sekiyama, A. et al. Technique for bulk Fermiology by photoemission applied to layered ruthenates. *Phys. Rev. B* **70**, 060506(R) (2004).
4. Gray, A. X. et al. Probing bulk electronic structure with hard X-ray angle-resolved photoemission. *Nat. Mater.* **10**, 759–764 (2011).
5. Gray, A. X. et al. Bulk electronic structure of the dilute magnetic semiconductor $Ga_{1-x}Mn_xAs$ through hard X-ray angle-resolved photoemission. *Nat. Mater.* **11**, 957–962 (2012).
6. Medjanik, K. et al. Direct 3D mapping of the Fermi surface and Fermi velocity. *Nat. Mater.* **16**, 615–621 (2017).
7. Tanuma, S. et al. Calculations of electron inelastic mean free paths. IX. Data for 41 elemental solids over the 50 eV to 30 keV range. *Surf. Interface Anal.* **43**, 689–713 (2011).
8. Lv, B. Q. et al. Observation of Weyl nodes in TaAs. *Nat. Phys.* **11**, 724–727 (2015).
9. Xu, S.-Y. et al. Discovery of a Weyl fermion state with Fermi arcs in niobium arsenide. *Nat. Phys.* **11**, 748–754 (2015).
10. Lv, B. Q. et al. Observation of three-component fermions in the topological semimetal molybdenum phosphide. *Nature* **546**, 627–631 (2017).
11. Kobayashi, M. et al. Unveiling the impurity band induced ferromagnetism in the magnetic semiconductor (Ga,Mn)As. *Phys. Rev. B* **89**, 205204 (2014).
12. Cancellieri, C. et al. Polaronic metal state at the $LaAlO_3/SrTiO_3$ interface. *Nat. Commun.* **7**, 10386 (2016).
13. Lev, L. L. et al. k-space imaging of anisotropic 2D electron gas in GaN/GaAlN high-electron-mobility transistor heterostructures. *Nat. Commun.* **9**, 2653 (2018).
14. Keqi, A. et al. Electronic structure of the dilute magnetic semiconductor $Ga_{1-x}Mn_xP$ from hard x-ray photoelectron spectroscopy and angle-resolved photoemission. *Phys. Rev. B* **97**, 155149 (2018).
15. Nemšák, S. et al. Element- and momentum-resolved electronic structure of the dilute magnetic semiconductor manganese doped gallium arsenide. *Nat. Commun.* **9**, 3306 (2018).
16. Trzhaskovskaya, M. B. et al. Dirac-Fock photoionization parameters for HAXPES applications. *Data Nucl. Data Tables* **119**, 99–174 (2018).
17. Trehan, R., Fadley, C. S. & Osterwalder, J. Single-scattering cluster description of substrate X-ray photoelectron diffraction and its relationship to Kikuchi bands. *J. Electron Spectrosc. Relat. Phenom.* **42**, 187–215 (1987).
18. Osterwalder, J., Greber, T., Hüfner, S. & Schlapbach, L. X-ray photoelectron diffraction from a free-electron-metal valence band: Evidence for hole-state localization. *Phys. Rev. Lett.* **64**, 2683–2686 (1990).
19. Herman, G. S., Tran, T. T., Higashiyama, K. & Fadley, C. S. Valence photoelectron diffraction and direct transition effects. *Phys. Rev. Lett.* **68**, 1204–1207 (1992).
20. Osterwalder, J., Greber, T., Aebi, P., Fasel, R. & Schlapbach, L. Final-state scattering in angle-resolved ultraviolet photoemission from copper. *Phys. Rev. B* **53**, 10209–10216 (1996).
21. Krüger, P., Da Pieve, F. & Osterwalder, J. Real-space multiple scattering method for angle-resolved photoemission and valence-band photoelectron diffraction and its application to Cu(111). *Phys. Rev. B* **83**, 115437 (2011).
22. Plucinski, L. et al. Band mapping in higher-energy x-ray photoemission: phonon effects and comparison to one-step theory. *Phys. Rev. B* **78**, 035108 (2008).
23. Papp, C. et al. Band mapping in X-ray photoelectron spectroscopy: an experimental and theoretical study of W(110) with 1.25 keV excitation. *Phys. Rev. B* **84**, 045433 (2011).
24. Braun, J. et al. Exploring the XPS-limit in hard X-ray angle-resolved photoemission spectroscopy by fully temperature-dependent one-step theory. *Phys. Rev. B* **88**, 205409 (2013).
25. Schlueter, C. et al. New HAXPES applications at PETRA III. *Synchrotron Radiat. News* **31**, 29–35 (2018).
26. Fadley, C. S. X-ray photoelectron spectroscopy: progress and perspectives. *J. Electron Spectrosc. Relat. Phenom.* **178–179**, 2 (2010).
27. Winkelmann, A., Fadley, C. S. & Garcia de Abajo, F. J. High-energy photoelectron diffraction: model calculations and future possibilities. *New J. Phys.* **10**, 113002 (2008).
28. Baba-Kishi, K. Z. & Dingley, D. J. Backscatter Kikuchi diffraction in the SEM for identification of crystalloghraphic point groups. *Scanning* **11**, 305 (1989).
29. Schönhense, G. et al. Momentum-transfer model of valence-band photoelectron diffraction. Preprint at http://arXiv.org/1806.05871 (2018).
30. Claessen, R. et al. Complete band-structure determination of the quasi-two-dimensional Fermi-liquid reference compound $TiTe_2$. *Phys. Rev. B* **54**, 2453–2465 (1996).
31. Krasovskii, E. E., Rossnagel, K., Fedorov, A., Schattke, W. & Kipp, L. Determination of the hole lifetime from photoemission: Ti 3d states in $TiTe_2$. *Phys. Rev. Lett.* **98**, 217604 (2007).
32. Herman, G. S. & Fadley, C. S. Inelastic photoelectron diffraction. *Phys. Rev. B* **43**, 6792(R) (1991).
33. Osterwalder, J., Greber, T., Hüfner, S. & Schlapbach, L. Photoelectron diffraction from core levels and plasmon-loss peaks of aluminum. *Phys. Rev. B* **41**, 12495 (1990).
34. Hussain, Z., Fadley, C. S., Kono, S. & Wagner, L. F. Temperature-dependent angle-resolved X-ray photoemission study of the valence bands of single-crystal tungsten: evidence for direct transitions and phonon effects. *Phys. Rev. B* **22**, 3750–3766 (1980).
35. Stewart, G. R. Measurement of low-temperature specific heat. *Rev. Sci. Instrum.* **54**, 1 (1983).
36. Chernov, S. V. et al. Anomalous d-like surface resonances on Mo(110) analyzed by time-of-flight momentum microscopy. *Ultramicroscopy* **159**, 463 (2015).
37. Fedchenko, O. et al. 4D texture of circular dichroism in soft-x-ray photoemission from tungsten. *New J. Phys.* **21**, 013017 (2019).
38. Kozina, X. et al. Development of hard X-ray photoelectron SPLEED-based spectrometer applicable for probing of buried magnetic layer valence states. *J. Electron Spectrosc. Relat. Phenom.* **211**, 12–18 (2016).
39. Pendry, J. B. Theory of Photoemission. *Surf. Sci.* **57**, 679–705 (1976).
40. Pendry, J. B., *Low Energy Electron Diffraction* (Academic Press, Imperial College London, 1974).
41. Choy, T.-S., Naset, J., Chen, J., Hershfield, S. & Stanton, C. A. database of fermi surface in virtual reality modeling language (vrml). *Bull. Am. Phys. Soc.* **45**, L36 (2000).

Acknowledgements

Sincere thanks are due to A. Oelsner (Surface Concept GmbH) for continuous support and to A. Winkelmann (Laserzentrum Hannover) for fruitful discussions. Funding by BMBF (projects 05K16UM1/Mainz and 05K16FK2/Kiel) and DFG through Transregio SFB TR173 Spin+X is gratefully acknowledged. We acknowledge DESY (Hamburg, Germany), a member of the Helmholtz Association (HGF) for the provision of experimental facilities. Parts of this research were carried out at P04 and P22.

Author contributions

S.B. and G.S. wrote the paper. S.B., K.M., D.V., S.C., H.-J.E. and G.S. set up and carried out the experiment and prepared the samples. B.S., H.-J.E., S.B. and K.R. performed the data evaluation. K.R. provided $TiTe_2$ samples. C.S., A.G., Y.M. and W.D. helped with the microscopy control unit and beamline P22. G.S. and H.-J.E. coordinated the project. All authors discussed the results and contributed to the writing of the manuscript.

Additional information

Supplementary information accompanies this paper at https://doi.org/10.1038/s42005-019-0208-7.

Competing interests: The authors declare no competing interests.

Reprints and permission information is available online at http://npg.nature.com/reprintsandpermissions/

Publisher's note: Springer Nature remains neutral with regard to jurisdictional claims in published maps and institutional affiliations.

Open Access This article is licensed under a Creative Commons Attribution 4.0 International License, which permits use, sharing, adaptation, distribution and reproduction in any medium or format, as long as you give appropriate credit to the original author(s) and the source, provide a link to the Creative Commons license, and indicate if changes were made. The images or other third party material in this article are included in the article's Creative Commons license, unless indicated otherwise in a credit line to the material. If material is not included in the article's Creative Commons license and your intended use is not permitted by statutory regulation or exceeds the permitted use, you will need to obtain permission directly from the copyright holder. To view a copy of this license, visit http://creativecommons.org/licenses/by/4.0/.

© The Author(s) 2019